BROOKHAVEN NATIONAL LABORATORY

BNL-222519-2021-JAAM

Controlled Organization of Inorganic Materials Using Biological Molecules for Activating Therapeutic Functionalities

M. Chandler, O. Gang

To be published in "ACS Applied Materials & Interfaces"

August 2021

Center for Functional Nanomaterials

Brookhaven National Laboratory

U.S. Department of Energy

USDOE Office of Science (SC), Basic Energy Sciences (BES) (SC-22)

DISCLAIMER

Controlled organization of inorganic materials using biological molecules for activating therapeutic functionalities

*Morgan Chandler, Brandon Roark, Mathias Viard, Brian Minevich, M. Brittany Johnson, Mehedi Hasan Rizvi, Thomas A. Deaton, Seraphim Kozlov, Martin Panigaj, Joseph Tracy, Yaroslava G. Yingling, Oleg Gang, Kirill A. Afonin**

M. Chandler, B. Roark, S. Kozlov, Prof. K. A. Afonin
Nanoscale Science Program
Department of Chemistry
University of North Carolina at Charlotte
Charlotte, NC 28223, USA
E-mail: kafonin@uncc.edu

Dr. M. Viard
Cancer and Inflammation Program,
Leidos Biomedical Research Inc.
Frederick National Laboratory for Cancer Research
Frederick, MD 21702, USA

B. Minevich, Prof. O. Gang
Department of Chemical Engineering
Columbia University
New York, NY 10027, USA

Prof. M. B. Johnson
Department of Biological Sciences
University of North Carolina at Charlotte
Charlotte, NC 28223, USA

M. H. Rizvi, T. A. Deaton, Prof. J. Tracy, Prof. Y. G. Yingling
Department of Materials Science and Engineering
North Carolina State University
Raleigh, NC 27695, USA

Dr. M. Panigaj
Institute of Biology and Ecology
Faculty of Science
Pavol Jozef Safarik University in Kosice
Kosice 04154, Slovak Republic

Prof. O. Gang
Department of Applied Physics and Applied Mathematics
Columbia University
New York, NY 10027, USA

Prof. O. Gang
Center for Functional Nanomaterials
Brookhaven National Laboratory
Upton, NY 11973, USA

Keywords: quantum dots, therapeutic nucleic acids, 3D lattices, programmable assembly, materials organization

Abstract: Precise control over the assembly of three-dimensional nano-composites offers a route to orchestrating processes in the biological environment in a manner similar to the complex spatial processes carried out by the cell itself. Using nucleic acids as programmable crosslinkers to direct the assembly of inorganic quantum dots (QDs), variations in assembly strategies are demonstrated for the formation of DNA-scaffolded QD lattices. Morphologies are evaluated via gel electrophoresis, transmission electron microscopy, and small-angle X-ray scattering while Dissipative Particle Dynamics modeling is used to predict the morphologies. The controlled assembly of 3D QD organizations is demonstrated in cells via the colocalized emission of multiple QDs in the lattice and their immunorecognition is assessed. The RNA interference inducers are also embedded into the components to be released only upon lattice assembly, which is demonstrated by specific gene silencing efficacy. The programmability and intracellular activity of QD lattices offer a strategy for nucleic acids to imbue structure and therapeutic function into the formations of complex networks of nanostructures.

1. Introduction

Non-random spatial organization at the subcellular and cellular levels and the principles that govern it are some of the most intricate avenues of biology. The compartmentalization of cellular processes and the three-dimensional (3D) arrangement of biochemical pathways has a profound impact on cellular life. The structural configuration of macromolecular complexes is a dynamic process wherein all organized conglomerates are built and dismantled dependingon the requirements of the cell. Therefore, the 3D organization of biomolecules has spatiotemporal characteristics. In addition, many biological structures exhibit the intrinsic ability of self-organization or self-assembly.[1]

Many 3D structures of biological origin include inorganic components (*e.g.*, hydroxyapatite, silica, magnetite, and calcite) that, together with organic material (*e.g.*,

proteins), form precise arrangements from the nano- to macroscale. The formation of hybrid complexes is precisely controlled by the organism and the final constructions are endowed with unique properties. These composite structures perform diverse functions: mechanical (*e.g.* bones, shells, dental tissues, *etc.*), magnetotactic (*e.g.* superparamagnetic particles in magnetotactic bacteria), piezoelectric (*e.g.* aragonite platelets in nacre), and optical (*e.g.* sponge spicule as optical fiber).[2] The organization of inorganic materials in various 3D nanostructures with various degrees of complexity mimics such biological approaches by combining components of distinct physicochemical properties for promising applications in imaging, sensing, drug delivery, and tissue engineering, to name a few. Generally, two approaches employing biomolecules can be applied for the 3D organization of nanoparticles involving inorganic material: top-down and bottom-up. In the top-down approach, inorganic structures of cellular origin such as a diatom's cell walls or viral particles can serve as templates for organization. Attachment to these template surfaces can be nonspecific, or microorganisms can be genetically engineered to express functional groups for selective interactions with nanoparticles or their adsorption with increased affinity.[3-5] The top-down methods for nanoparticle formation on the cellular scale are intrinsically less controllable and depend on the structure/shape of the template. Therefore, the *de novo* organization of inorganic particles by natural polymers such as polypeptides and nucleic acids offers advantages for regulating the assembly behavior[6]. However, despite its attractiveness for biotechnology, the bottom-up assembly of inorganic elements controlled by rationally designed organic molecules is challenging.

Since the organization of most of the inorganic material in assemblies is performed by proteins specific to minerals (*e.g.*, bone morphogentic proteins in bones, or amelogenin in enamel growth[7,8]), it is tempting to use engineered peptides to create artificial 3D shapes. Indeed, several groups have attempted to develop bottom-up methods for the assembly of nanoparticles with the organization of inorganic material driven by self-assembly of *in vitro* evolved peptides

specific to inorganic elements such as metals, oxides, or semiconductors.[9,10] The limiting diversity of protein-based geometries can be additionally improved by the combination of engineered inorganic specific-peptides with nucleic acids. In this DNA-peptide-metal nanoparticle arrangement, DNA provides symmetrical scaffolding for peptides with affinity to the nanoparticle (*e.g.*, the two-dimensional grid based on self-assembling cross-tile DNA template with periodically linked peptides). This model represents artificial biomineralization, where a single peptide molecule binds one gold nanoparticle.[11]

Nucleic acids are materials with programmable, dynamic, and environmentally responsive functional components for hybrid nanoparticles. Due to their simple primary structure and known rules that guide the formation of their secondary and tertiary conformations, nucleic acids are a superior material for scaffolding in comparison to proteins or other biopolymers. The synthesis of nucleic acids is relatively easy and scalable. In addition, by using a bottom-up strategy, we can control and rationally program the 3D shape of nucleic acid-based nanoparticles from nano- to microscale.[12,13] Several experiments have demonstrated the versatility of nucleic acid scaffolds to display functional DNA/RNA motifs with promising applications in biotechnology or biomedicine. *In vivo* transcribed RNA scaffolds with embedded aptamers have the potential to co-localize enzymatic pathways that result in enhanced metabolic production, while multivalent DNA nanostructures displaying bi-specific aptamers have been shown to facilitate cell-cell interactions[14-17] In addition to organizing proteins via aptamers, RNA is a platform for spatial arrangements of intrinsic functionalities such as siRNAs with applications in the modulation of gene expression.[13,18] The ability to dynamically respond to the environment makes nucleic acids an attractive biomaterial for tailormade structures with desired responsiveness. In the past decades, a wide array of artificially designed dynamic nucleic acid assemblies have been shown to react on the broad spectrum of physicochemical or biological stimuli (*e.g.* pH, light, ion concentration, small metabolites, enzymes, or nucleic acid strands).[19-26] As was recently demonstrated in a hydrogel,

stimuli-responsive DNA may also provide switchable control over the spatial organization of scaffolds.[27]

In a pioneering study which tested the potential of nucleic acids to arrange macrostructures from nanostructures, Mirkin *et al.*, used colloidal metal particles. In their experimental model, colloidal gold nanoparticles coupled to oligonucleotides aggregated upon the addition of complementary DNA strands. The macroscopic aggregation was shown to be a reversible reaction, driven by the thermal denaturation of nucleic acids.[28] Later, the idea of nanoparticle assembly mediated by DNA was extended with the use of rationally designed oligonucleotides that can control the crystallization of gold nanoparticle–oligonucleotide conjugates through the interactions of programmable base-pairing sequences into various crystal structures. The position of the metal nanoparticles in the crystal can be influenced by linker sequence with or without flexor.[29] A higher degree of control over assembly can be further achieved by introducing an asymmetric functionalization of particles where oligonucleotides are specifically localized on particles and allow for the assembly of unique heterostructures.[30]

In addition to gold-DNA constructs, DNA oligonucleotides have been conjugated to other inorganic particles with distinct physicochemical properties.[31] In particular, quantum dots (QDs) attract increasing attention for the development of nano-theranostic concepts for simultaneous diagnostics and therapy.[32] Colloidal QDs are semiconductor nanocrystals endowed with physicochemical characteristics which allow for their easy readout and quick analysis. In comparison to organic fluorophores, the QDs are strongly luminescent, have increased stability, higher brightness, and resistance to photo bleaching as well as narrower and symmetric fluorescence spectra with tunable colors controlled by their size. Using DNA for linking, QDs can be utilized to create assemblies with controlled bonding, valency, and photoluminescence.[33] Over the last two decades, numerous studies have developed approaches for modifying the surface of QDs with biomolecules for the attachment of functionalized

moieties such as DNA/RNA oligonucleotides, antibodies, peptides, *etc*[34]. Almost exclusively as optical labels, functionalized QDs have found many applications in biosensing and bioimaging.[35-37] Instead of fluorescent dyes, QDs can be conjugated to aptamers for the visualization of aptamer binding and subsequent intracellular trafficking.[38] Aptamer-QD complexes have been examined to detect various targets, from simple metal ions, drugs, or toxins to proteins.[39] An RNA aptamer linked to QDs has also been shown as an alternative for protein detection in Western blot analysis.[40] The specific binding of engineered endonuclease-deficient genome editing proteins (*e.g.* transcription activator-like effectors (TALEs) or CRISPR/Cas9 labeled with QDs) has been demonstrated as a viable visualization strategy of single genomic loci in live human cells.[41,42]

Various strategies of visualizing viral components with QDs offers opportunities for understanding the virus life cycle on a molecular level through the real-time observation of viral trafficking, molecular interactions, *etc.* Viral tracking is mediated either by indirect labeling using viral protein-specific antibodies conjugated to QDs, or by the direct attachment of streptavidin-coated QDs to viral proteins fused to biotinylated peptide tags.[43-47] In addition to virus tracking, QDs have been used to track plasmid DNA after transfection as well as endocytic pathways with DNA nanoparticles linked to different endocytic ligands.[48,49] MicroRNAs (miRNAs), which are small non-coding RNAs that participate in the regulation of gene expression, are promising objects for sequence-specific detection by QD-oligonucleotides. The biosensing is based on the base-pairing between the target miRNA and oligonucleotide with several means of signal outcome such as by luminescence, triggering its shutdown, or measurements of changes in intensity.[50] The sensitivity of detection can be modulated by other functional molecules such as DNAzymes or exonucleases.[51,52] Similarly, amplification of the signal can be significantly improved by assembling gold nanoparticles with QDs mediated by DNA oligonucleotides. The *in vivo* presence of specific disease-related miRNAs catalyzes dis-assembly of complexes leading to signal release. The process is triggered by toehold

interactions of miRNA with a DNA linker that subsequently base-pairs with exogenously delivered "fuel" DNA oligonucleotides.[53] Furthermore, DNA strand displacement-driven dynamic assemblise of binary and ternary multicolor QD complexes can create all seven basic logic gates (OR, AND, NOR, NAND, INH, XOR, XNOR) that could be applied in logical biosensing of therapeutically interesting nucleic acids.[54] Although most biosensing and bioimaging applications of QDs rely on the measurement of changes in fluorescence (color or intensity), QDs offer additional properties for detection. The fluorescence intermittency or blinking is an inherent random fluctuation between ON (bright) and OFF (dark) states of individual QDs.[55] The phenomenon is observable only in a single QD, while in aggregated QDs, the signal is semi-steady. Therefore, differences in signal between the single QDs versus an accumulated group of QDs can be distinguished and used for the detection of target molecules as has been reported by the first proof-of-concept study. The principle of this strategy is strand displacement triggered by target sequence, leading to the re-association of two split biotinylated oligonucleotides that subsequently promote the arrangement of streptavidin-decorated QDs into lattices. The transition from single state to 3D assembly flattens blinking to a continuous signal.[56]

Hybrid inorganic-organic component structures have been widely recognized in many proof-of-concept studies as interesting materials for theranostic applications. The inorganic components of the nanotherapeutics are endowed with unique physicochemical properties with relevant diagnostic or therapeutic potential such as magnetic properties, exceptional luminescent characteristics, and inducibility of physical therapeutic effects (*e.g.*, hyperthermia in target tumor cells). However, many challenges are awaiting optimization through solubility, excretion, circulation time, barrier penetration, target specificity/efficiency, and, last but not least, biocompatibility/toxicity [57].

From this standpoint, the connection of inorganic particles with nucleic acids as a major organic constituent can be a determinative driving force for addressing current obstacles. Yet

currently speculative, future research may lead to the development of hybrid nanoparticles where reversible states between assembly and disassembly of the nucleic acids components can improve the transfer of nanoparticles to target organ sites, including their cumulative performance after delivery. Nucleic acids may dynamically respond to physicochemical or biological patterns of the surrounding microenvironment, change their structures, and thereby also subsequently change the dimensions and sizes of hybrid assemblies. Hypothetically, hybrid inorganic-nucleic acid 3D structures may travel through the blood system in a semi-aggregated state to avoid excretion (renal clearing) and dissociate to a desired extent upon specific binding to target cell receptors as mediated by aptamers (aptazymes). Subsequently, upon successful directed or passive endosomal escape, target molecules (*e.g.* nucleic acid, protein or metabolite) would trigger particular or combined functionalities (*e.g.* RNA interference, DNAzymes, decoys, anti-miRs, *etc.*). Additionally, depending on the nature of inorganic components, a physicochemical response can be induced autonomously by the cellular environment or by an external force (*e.g.* magnetic field, illumination, *etc.*). The final multifunctional outcome could resemble already described monodisperse composite nanoparticles, minimally allowing for targeted imaging, therapy, and sensing. For example, functionalized QDs with the RNA aptamer targeting prostate cancer cells can deliver doxorubicin (Dox) intercalated in the double-stranded part of the aptamer. In this form, both QD and Dox are fluorescently in an OFF state, but the signal turns ON when Dox is released inside the diseased cells.[58] Similarly, the specific detection of a target (thrombin) by aptamer-QD particles induces aptamer refolding, leading to a decrease in signal of DNA-intercalating dyes and increase in signal of QDs.[59] Another promising application of biodegradable inorganic-organic 3D assemblies is scaffolding in tissue engineering where nanoscaffolds can regulate cell adhesion and differentiation *in vitro* towards improvement in transplantation.[60]

In this work, we set out to describe the functional possibilities of regulation of nucleic acid-based reconfigurable scaffolds by a simple visual readout mediated by QDs. This system

uses both RNAs and biotinylated DNAs as a means to drive the 3D organization of streptavidin-decorated QDs. We first compared several approaches for the formation of bioresponsive reconfigurable QD 3D assemblies using QDs linked to complementary single-stranded (ss)DNAs, combined with double-biotinylated DNA duplexes, or decorated with DNA/RNA hybrids that re-associate to release Dicer Substrate (DS) RNAs. The resulting assemblies from each method of assembly were extensively characterized via electrophoretic mobility shift assays (EMSA), transmission electron microscopy (TEM), and small-angle X-ray scattering (SAXS). Next, we studied relative cellular uptake efficiencies, immunostimulatory properties, and intracellular co-localization of the 3D lattices and their individual components. We have shown that intracellular formation of QD lattices in human breast cancer cells releases DS RNAs and, upon dicing, triggers specific gene silencing.

2. Results and Discussion

The composition of nucleic acids and the manner in which they are introduced offers versatility in QD lattice formation that results in 3D assemblies with various sizes, kinetics, and functionalities. Three methods of QD lattice assembly were evaluated. First, through incubation of double-stranded (ds)DNA oligonucleotides with single biotin present on both ends of each duplex, binding with streptavidin-coated QDs drives the rapid (~30 seconds) formation of assembled structures (**Figure 1A**). As seen in the agarose gel, the QDs alone begin to migrate upon addition of an ssDNA. However, full assembly into larger-scale organization over time results in morphologies which are too large to enter the gel and can thus be observed in the loading wells only. In comparison, if individual complementary DNA strands are added separately to QDs and then combined, it takes closer to 30 minutes for the aggregate to fully assemble (**Figure 1B**). As the third approach, QDs were separately conjugated to complementary dsDNA/RNA hybrid duplexes via the biotinylated DNA. Once added together, a 12 nt-ssDNA toehold was utilized in order to initiate the isothermal strand displacement

reaction that promotes the formation of DNA duplexes while releasing the RNA sequences to form functional DS RNAs (**Figure 1C**). The highest proportion of assembled lattices and released DS RNAs was achieved after 60 minutes. In all three strategies of lattice formation, the addition of DNase to assembled 3D structures completely voided the formation of assembled structures, resulting in the increased mobility of QDs.

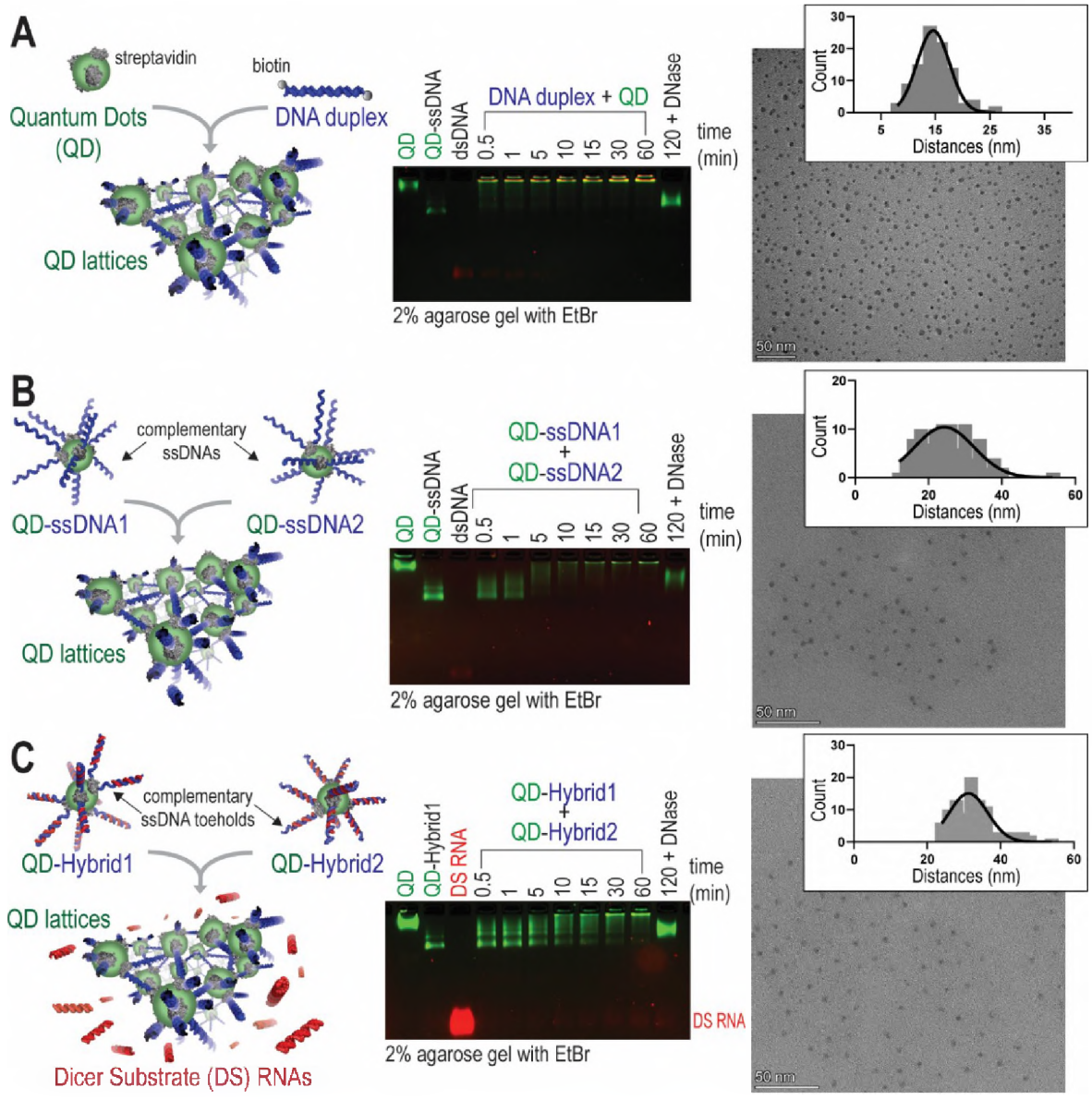

Figure 1. Various protocols of QD lattice formation. Agarose gels show the kinetics of QD lattice formation. TEM images depict the assembled lattices, with the distribution of center-to-center distances shown in the histogram. (**A**) QDs mixed with double-biotinylated DNA duplexes. (**B**) QDs decorated with complementary ssDNA. (**C**) QDs decorated with RNA-DNA hybrids that re-associate via the complementary ssDNA toehold interaction and release Dicer Substrate (DS) RNAs.

All three methods to form QD assemblies were assessed via TEM. Analysis of the center-to-center distances between a given QD and its three nearest neighbors was assessed to compare QD distributions (**Figure S1**). For dsDNA duplex-driven QD lattice assembly, the mean center-to-center distance was 17.84 ± 1.37 nm. For ssDNA-driven QD lattice assembly, the mean center-to-center distance was 26.76 ± 1.82 nm. Finally, for hybrid-driven QD lattices, the mean center-to-center distance was 26.31 ± 4.31 nm. The distribution of distances for 100 QDs are shown for each TEM image in **Figure 1A-C**.

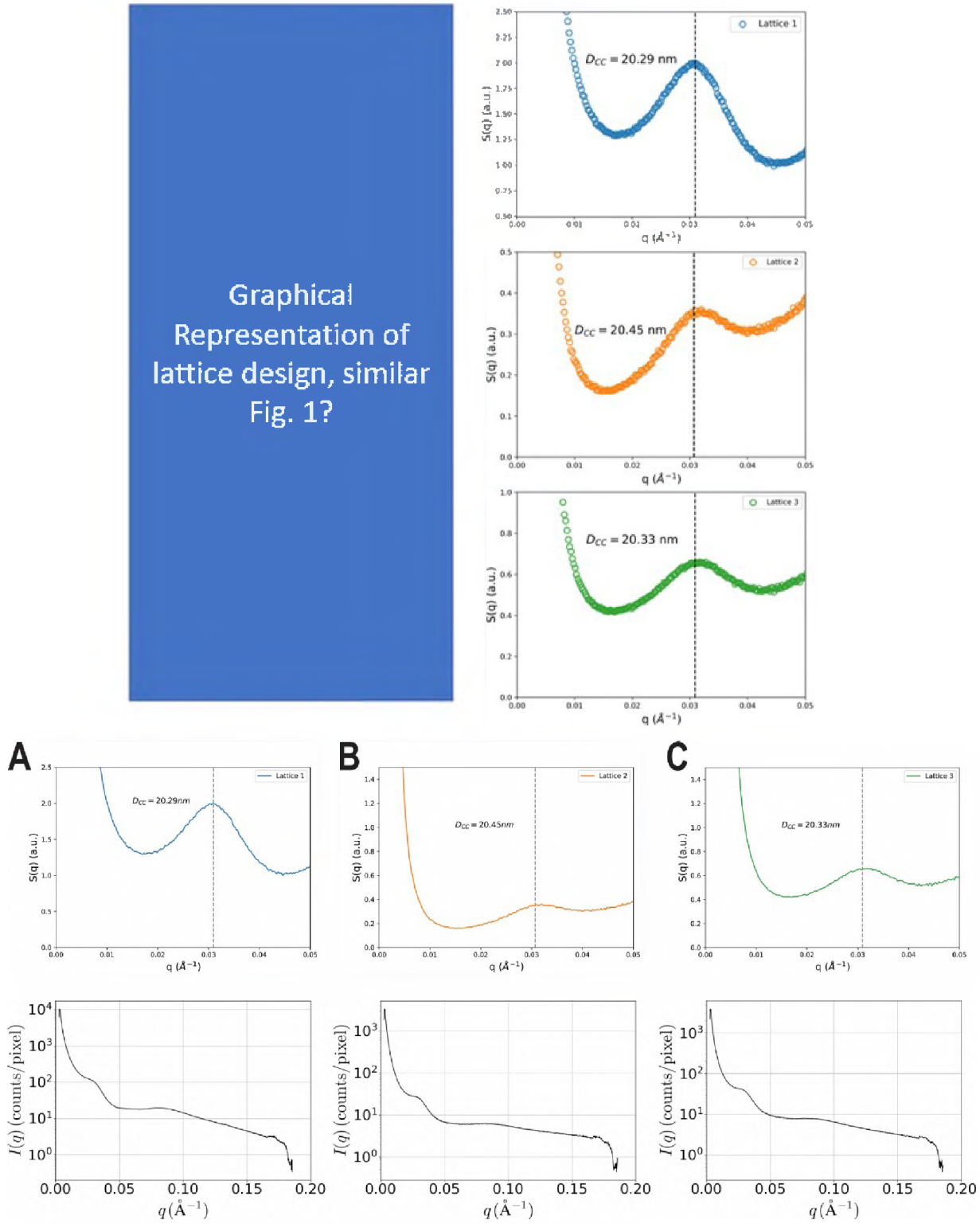

Figure 2. SAXS analysis of the assembly of (**A**) dsDNA-, (**B**) ssDNA-, and (**C**) hybrid DNA/RNA-driven QD lattices. For each lattice, the Structure Factor Plot (top) and Intensity Profile Plot (bottom) are shown.

Given the three-dimensional morphologies of the assemblies of the QDs in their native state for each of the assembly strategies described previously, synchrotron based small-angle

x-ray scattering (SAXS) was utilized for probing the structures of each of these systems *in-situ*. The scattering profiles for each of the designs showed a single broad peak as a function of the scattering vector, q, which corresponds to a disordered, aggregate system with a characteristic average center-to-center (D_{CC}) distance of the assembled QDs. Figure 2 summarizes the structure factor plots, $S(q)$, for each of the designs and the corresponding real-space distances are indicated on the respective plots based on the center of the peak fit with a Lorentzian function. For the dsDNA-, ssDNA-, and hybrid-driven QD lattices, these center-to-center distances were calculated to be 20.29 nm, 20.45 nm, and 20.33 nm, respectively. Compared to the values derived from TEM images, the values for the dsDNA-driven QD lattice were the most highly similar, differing only by 2.45 nm between averages. The averages of the two other methods of lattice assembly are also considered to be in agreement. Additional SAXS plots are available in **Figure S2 and S3**.

In addition to experimental approaches, computational modeling techniques offer a complimentary level of insight into how variables in the assembly result in changes in its organization. Here, the mesoscale modeling technique Dissipative Particle Dynamics (DPD) presents the opportunity to understand these materials on the size and time scales relevant to their assembly. DPD achieves these scales by using a soft potential that pairs hydrodynamics and the exclusion of volume to considerably increase computational efficiency as it compares to atomistic scale simulations.[61,62] The technique has shown success modeling an array of semi-dilute polymer-based material assembly including block copolymers, polyelectrolytes, and DNA[63-67]. Computational modeling of QD and DNA lattices provided a couple of key insights into the driving forces of the resulting morphologies. The initial system (**Figure 3A**) consists of 24 QDs which are decorated with 12 ssDNAs each. **Figure 3B** are snapshots of the final morphologies of the simulations conducted as a function of length and salt concentration. As length increases across any of the salt concentrations, the decorated quantum dots have an increased willingness to pack versus assembling in a more linear fashion for the shorter DNA.

This is quantified in the int-RDF of the quantum dot center of mass in **Figure 3C**, where each DNA length is averaged and then compared against the other lengths simulated. As the DNA length increases, the quantum dots spread out more. However, they do not spread out nearly as proportional as the length of the DNA increases. This results in the more packed configurations that are seen in the phase diagram in **Figure 3B**. Lastly, it is worth noting that while salt was varied across a wide spectrum of concentrations, it did not play nearly as much of a role in the morphology as the DNA lengths.

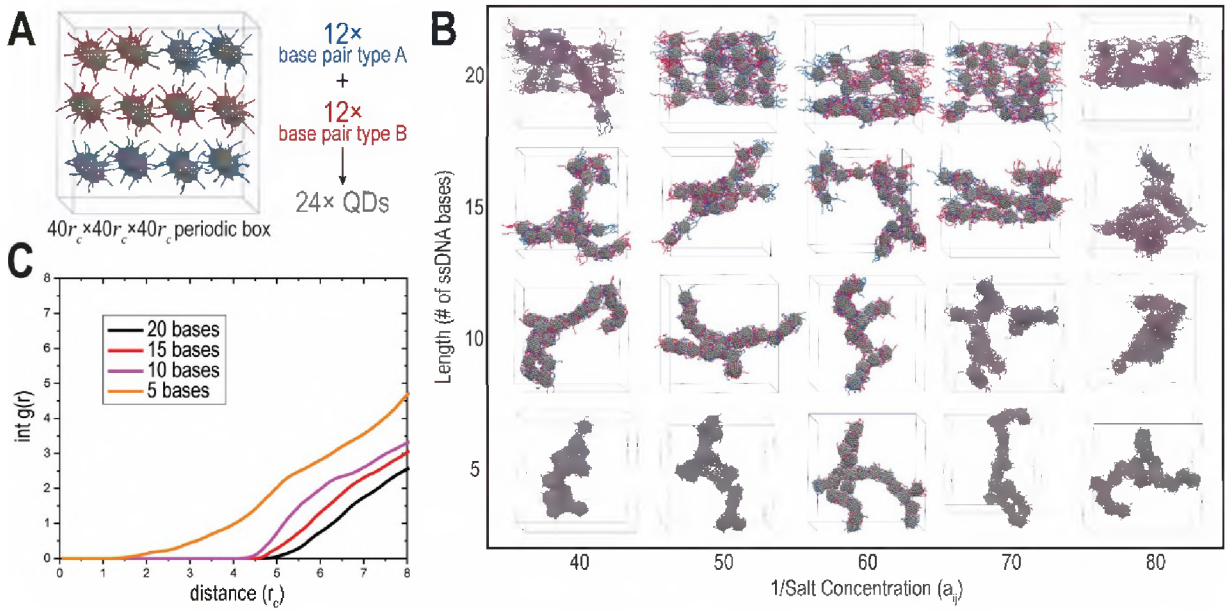

Figure 3. Computational modeling of QD-DNA formations. (**A**) Snapshot of initial DPD configuration. (**B**) Phase diagram of assembled QDs as a function of salt and length. (**C**) Integration of the radial distribution function of averaged lengths.

To fully take advantage of the programmable assemblies of inorganic QDs, assembled lattices were introduced into cells. Their relative uptake and intracellular assembly in MDA-MB-231 human breast cancer cells were assessed by separately introducing QDs carrying complementary DNA/RNA hybrids. Cells were then visualized via fluorescence microscopy and flow cytometry (**Figure 4A**). Micrographs labeled a-d correspond with the geometric mean fluorescence intensity (gMFI) shown to the right, wherein the stepwise introduction of materials for their intracellular assembly resulted in higher gMFI than for either QD component or pre-assembled QD lattices. To confirm that the cognate QDs can form intracellular lattices and thus

co-localizing inside cells, QD545 and QD605 carrying complementary hybrid DNA/RNA duplexes were introduced and the cells were analyzed by confocal microscopy (**Figure 4B**). The co-localization of each QD emission as shown on the superposition image (1+2+3) demonstrates the heterogenous assembly of lattices composed of both QDs and confirms the assembly of lattices in cells. Additional confocal microscopy images of the co-localization studies are shown in **Figure S3**.

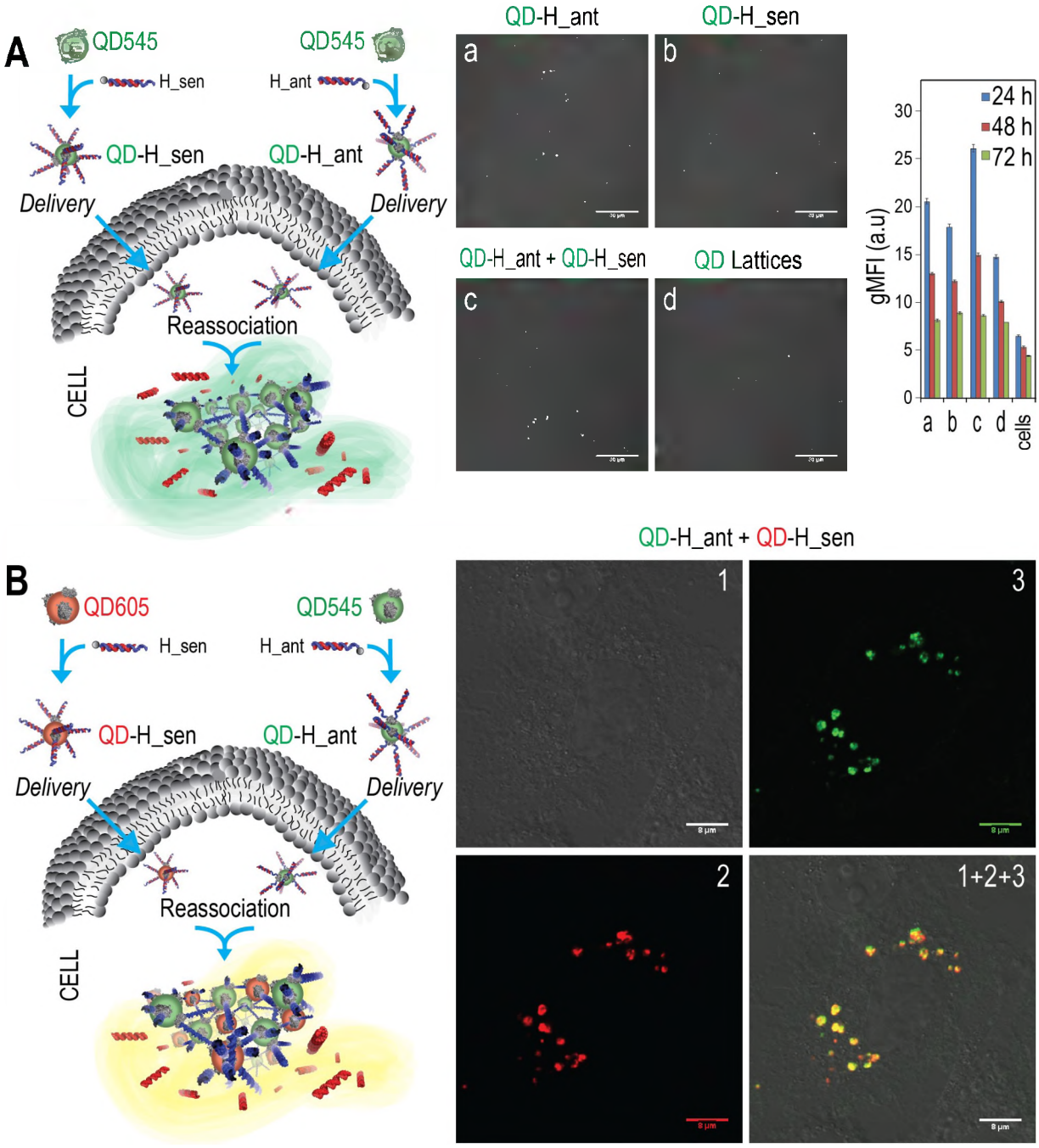

Figure 4. Relative uptake efficiencies and intracellular co-localization experiments. (**A**) Uptake of functionalized QD545 was analyzed by the fluorescence microscopy and flow cytometry. (**B**) Co-localization of QD545 (green)

and QD605 (red) entering the composition of QD lattices as analyzed by confocal microscopy. Image numbers correspond to: (1) differential interference contrast (DIC), (2) QD605 emission, and (3) QD545 emission. Image (1+2+3) is the superposition of three different images.

With uptake established, the potential for functional therapeutics imbued into the DNA/RNA lattice approach were further investigated. QDs carrying complementary hybrid duplexes were transfected stepwise into MDA-MB-231 cells engineered to express green fluorescent protein (GFP). The RNA sequences were designed to assemble into DS RNAs upon the reassociation of QDs inside the cell (**Figure 5**). With either QD and hybrid alone, the cells remained fluorescent with the expression of GFP. However, when both QDs were introduced to cells, the intracellular QD lattice formation was shown to result in the silencing of GFP assessed after 72 hours. Flow cytometry was used to confirm a statistically significant reduction in gMFI as a result of the lattice assembly. In timecourse studies, silencing with 10 and 20 nM QD lattice was observed even after up to 14 days (**Figure S4**).

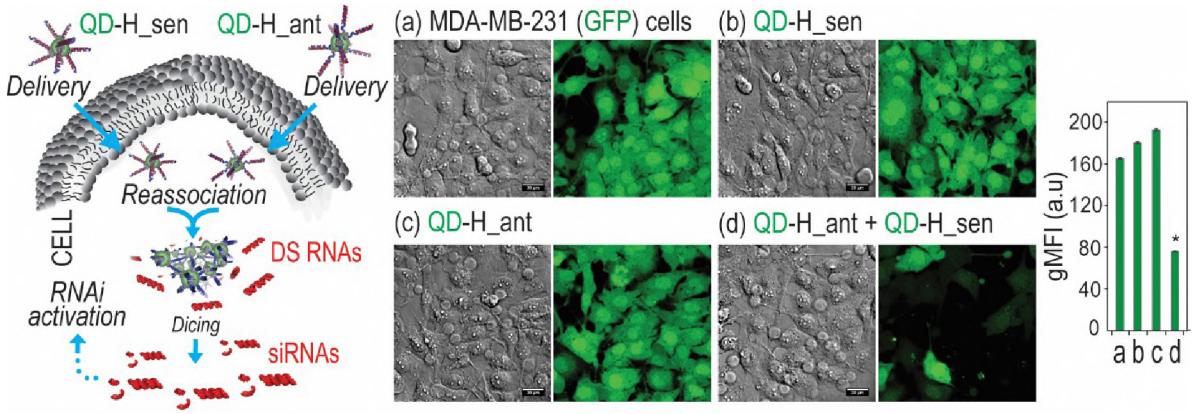

Figure 5. Activation of RNA interference in human breast cancer cells upon QD lattice formation. Intracellular QD lattice formation releases DS RNAs that trigger specific gene silencing upon dicing. Three days after the co-transfection of cells with QDs decorated with cognate hybrids, GFP silencing was confirmed by fluorescent microscopy and statistically analyzed with flow cytometry. Error bars denote ± SEM. Statistically significant results are indicated with asterisks (* = p-value < 0.05).

As a last step to confirm the downstream biological applications of these materials, their immunostimulation in cell lines was assessed. Hybrid duplexes and their reassociation were compared with free QDs, QDs with hybrid duplexes, and the reassociation of hybrid duplexes

when one (QD-H_sen+H_ant) or both (QD lattice) hybrids were bound to QDs. The relative production of cytokines hIL-1β, hIL-6, hIL-8, and hIFN-β in the human microglia-like cell like hHμ were assessed as normalized to cells treated only with Lipofectamine 2000 (L2K), which was used as a carrier (**Figure 6**). Overall, no components of the lattice assembly were identified as potent immune activators. Besides the control, QD-Hybrid1 showed the only statistical significance in regards to relative hIL-1β activation. The same panel of cytokines was also investigated for a human astrocyte-like cell line, U87 (**Figure S5**), in which no conditions demonstrated statistically significant immune stimulation.

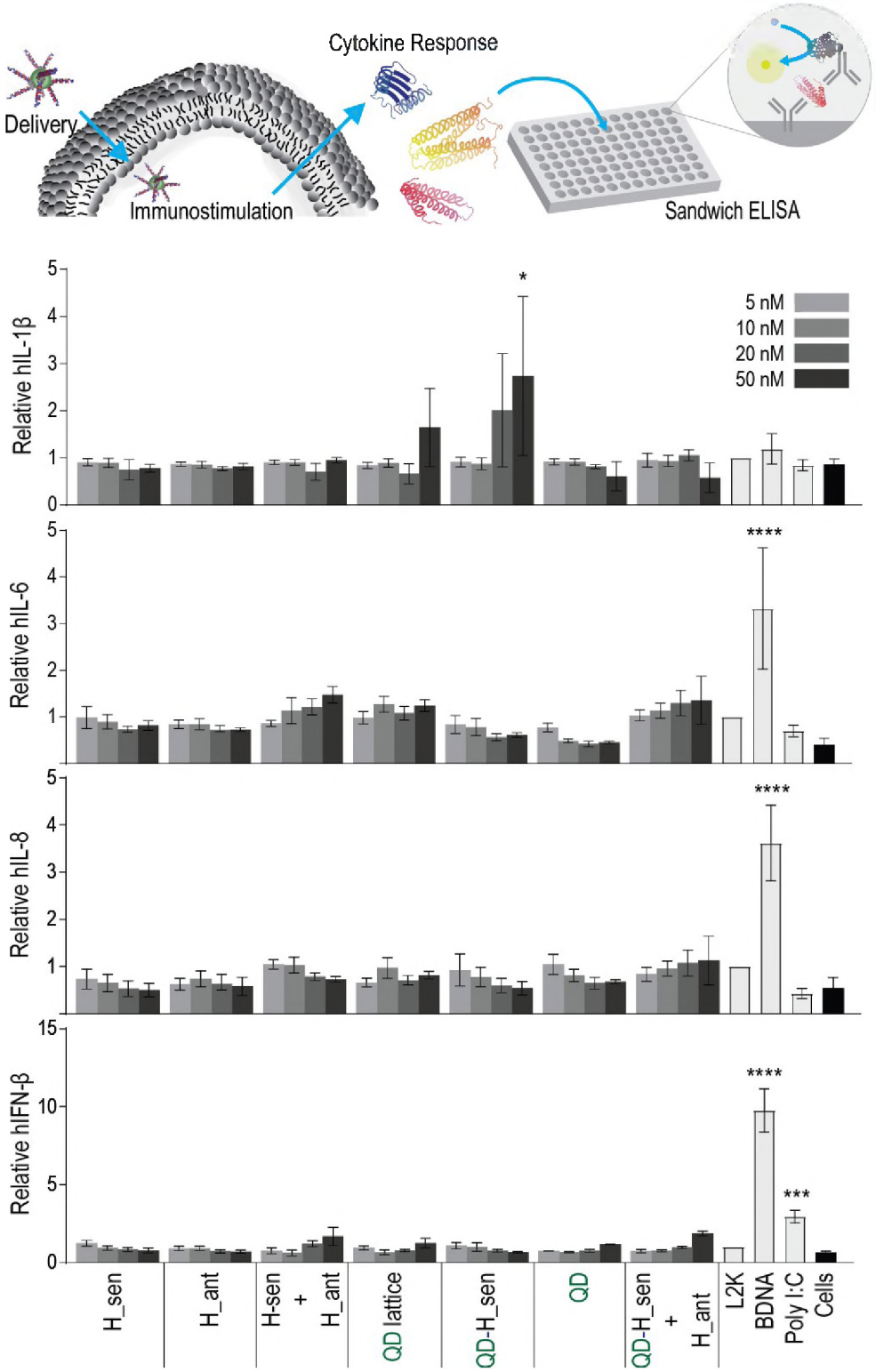

Figure 6. Immunostimulatory activity of QD lattices. A human microglia-like cell line (hHμ) was transfected and cell supernatants were collected 24 hours later. Levels of hIL-1β, hIL-6, hIL-8, and hIFN-β were assessed by ELISA. Error bars denote ± SEM. Statistically significant results are indicated with asterisks (**** = p-value < 0.0001, *** = p-value <0.001, * = p-value <0.05).

The colocalization of QDs 545 and 605 within a human breast cancer cell line demonstrates the assembly of lattices directly within the cellular environment, which is further validated by the significant fold knockdown of GFP in expressing cells via RNA interference

upon lattice formation. Importantly, QD lattices and their components do not invoke a significant difference in the production of cytokines, which makes this theranostic approach feasible on top of biosensing. While QDs alone exhibit narrow emission which is advantageous for tracking, assemblies of QDs offer more opportunities for sensing parameters.[56] For example, one avenue is that the centrifugation of assembled lattices results in the formation of a precipitate, while individual monomers show no precipitation (**Figure S6**).

Precise control over the assembly of complex networks of materials requires the coordination of all the individual components. Nucleic acids offer a straightforward route to scaffolding due to their programmable basepairing, but also allow for biologically relevant sequences to be implemented for therapeutic applications, as demonstrated here with the incorporation of DS RNAs. While three methods of assembly were demonstrated, their characterization shows similar morphologies despite variations in their kinetics. Based on the predicted DPD models, variations in morphologies can also be achieved by changing the lengths of DNAs in the lattice composition, which could also allow for other functional nucleic acids to be imbedded.

3. Experimental Section

Sequence design and preparation: DS RNAs designed against GFP and their complementary DNA sequences with 12 nt toeholds were purchased from Integrated DNA Technologies (IDT), as shown in previous work.[68] All sequences are listed in the Supporting Information. Oligos were diluted in endotoxin-free HyClone™ HyPure Cell Culture Grade Water (Cytiva) before use.

Assembly of QD lattices: QDs (Qdot™ 545 ITK™ Streptavidin Conjugate Kits from Invitrogen™) were assembled with either dsDNA, ssDNA, or DNA/RNA hybrid duplexes in endotoxin-free water with all QDs at 100 nM final concentration.

For (DNA duplex + QD) lattice: DNA duplexes were assembled by adding DNA oligos in an equimolar ratio. The sample was heated at 95°C for two minutes before assembly buffer (final concentration of 89 mM tris-borate (pH 8.2), 50 mM KCl, 2 mM $MgCl_2$) was added, followed by incubation at room temperature for 20 minutes. Afterwards, QDs were added with DNA duplex at a 1:10 QD:duplex molar ratio and incubated at 37 °C for 30 minutes.

For (QD+ssDNA1)+(QD+ssDNA2) lattice: QDs were assembled in two separate tubes with each DNA oligo in a 1:10 QD:DNA molar ratio in assembly buffer. Samples were incubated at 37°C for 20 minutes. Afterwards, the contents of the two tubes were mixed at a 1:1 volumetric ratio and incubated at 37 °C for 30 minutes.

For (QD+H_sen)+(QD+H_ant) lattice: Hybrid DNA/RNA duplexes were assembled in two separate tubes: H_sen ("DNA for Sense_12_Biotin" + "RNA Sense") and H_ant ("DNA for Antisense_12_Biotin" + "RNA Antisense.") The Hybrid Duplexes were prepared by adding their constituent oligos in an equimolar ratio, heating at 95°C for two minutes, and adding assembly buffer, followed by incubation at room temperature for 20 minutes. QDs were added to each separate Hybrid Duplex tube in a 1:10 QD:duplex molar ratio and incubated at 37 °C for 30 minutes. Afterwards, Hybrid Duplexes were mixed in a 1:1 volumetric ratio and incubated at 37 °C for 60 minutes.

Electrophoretic mobility shift assays (EMSA): To confirm assembly, QD lattices were visualized on a 2% agarose gel stained with 0.5 μg/mL ethidium bromide. Gels were run in 89 mM tris-borate, 2 mM EDTA (pH 8.2) for 20 minutes at 220 V, then visualized on a Bio-Rad™ ChemiDoc MP Imaging System using the Multichannel protocol for QD525 (used to view QD545) and QD605 (used to view ethidium bromide).

For EMSAs of the kinetics of lattice formation as shown in **Figure 1**, QD lattices were assembled in 40 μL volumes as described and incubated at 37 °C over a period of 120 minutes as previously shown.[56] At the 0.5, 1, 5, 10, 15, 30, and 60 minute timepoints, 4 μL of assembling QD lattice were added to 4 μL of agarose loading buffer (30% glycerol, 0.25% bromophenol

blue, 0.25% xylene cyanol) in a tube, which was immediately placed on dry ice. At the 90 minute timepoint, 1 µL of RQ1 RNase-Free DNase (Promega) was added and allowed to incubate for an additional 30 minutes. Samples were visualized via EMSA as above by loading 4.0 µL of each sample per well by descending timepoint, along with controls.

Precipitation of QD Lattices: 50 µL samples of assembled lattice (with final QD concentration of 100 nM) or controls were centrifuged at 4 °C for 5 minutes at 10, 5, 2.5, or 1 G on a ThermoScientific Sorvall Legend Micro 21R Centrifuge. All precipitates were immediately visualized on a Bio-Rad™ ChemiDoc MP Imaging System.

TEM: Mehedi/Dr. Tracy Three representative images (**Figure S1**) chosen from each of the three methods of lattice formation were assessed in ImageJ using the ND ImageJ plugin to calculate center-to-center distances[69,70]. The radius (r_1) of each identified QD point was calculated as half the average of the width plus height. The distances from the edge of each QD to its three nearest neighbors (d) were averaged along with the average wall thickness (r_2) of the three nearest neighbors using the ND ImageJ plugin. To calculate each center-to-center distance, r_1, r_2, and d were added together and averaged for the first 100 events in each of the three TEM images. The three average center-to-center distances were then averaged and the standard error of the mean (SEM) was calculated based on n=3 images. For visualizing the distribution of center-to-center distances, the first 100 events in each of the images shown in **Figure 1** were plotted in a histogram and fit with a Gaussian distribution using GraphPad Prism version 9.0.0 for Windows, GraphPad Software, San Diego, California USA, www.graphpad.com.

SAXS: 40 µL of assembled lattice samples were loaded into capillary tubes and then sealed with wax. Samples were then measured under vacuum conditions at the Complex Materials Scattering beamlines at the National Synchrotron Light Source II at Brookhaven National Laboratory (Upton, NY). The 2D scattering data was collected on area detectors downstream of the sample. The 2D data was then integrated into one-dimensional I(q) curves

as a function of the scattering vector, q. The scattering vector is defined as $q = \frac{4\pi \sin\theta}{\lambda}$, where λ and θ is the wavelength of the incident X-rays and the full scattering angle, respectively. The resultant 1D curves span from roughly 0.03 nm^{-1} to 1 nm^{-1} with a resolution of 0.002 nm^{-1}. The experimental S(q) was calculated by dividing the obtained I(q) 1D curves by the form factor or P(q) corresponding particles used in the sample preparation. Additional details of the experimental setup are provided in the SI. After the S(q) curves were obtained, peaks were fit with a Lorentzian distribution to obtain the center of the peak which was used to calculate to calculate the center-to-center distances (D_{CC}) of the assembled particles, where $Dcc = \frac{2\pi}{q}$.

Dissipative Particle Dynamics: As previously stated, DPD is a proven mesoscopic method to modeling materials such as DNA. To achieve mesoscales, DPD utilizes a coarse-grained approach where groups of atoms, among which their specific interactions are outside the scope of concern, are lumped together to form one bead. The movements of the DPD beads are dictated by Newton's equations of motion and are subject to a soft potential comprised of three non-bonded pairwise components along with a harmonic bonded spring force,

$$\frac{dr_i}{dt} = v_i, \; m_i \frac{dv_i}{dt} = \sum_{j \neq i} f_{ij}, \; f_{ij} = F^C_{ij} + F^D_{ij} + F^R_{ij} + F^S_{ij} \tag{1}$$

where r_i, v_i, and m_i are the position, velocity, and mass of bead i. The force between two beads, f_{ij}, is comprised of three non-bonded components including a conservative force, FC_{ij}, dissipative force, FD_{ij}, and random force, FR_{ij}. They are resolved by

$$F^C_{ij} = \begin{cases} a_{ij}\left(1 - \frac{r_{ij}}{r_c}\right) r_{ij}, & r_{ij} < r_c \\ 0, & r_{ij} > 0 \end{cases} \tag{2}$$

$$F_{ij}^{*} = -\gamma\omega^{*}(r_{ij}\cdot r_{ij})\cdot v_{ij}$$

(3)

$$F_{ij}^{+} = \sigma\omega^{+}(r_{ij})\theta_{ij}\Delta t^{-1/2}r_{ij}$$

(4)

where a_{ij} is the maximum repulsion between the two beads i and j, r_{ij} is the magnitude of distance between i and j, $v_{ij} = v_i - v_j$, and r_{ij} is the unit vector along j to i. γ and σ_D are coefficients that determine the amount of the dissipative and random forces, where

$$\gamma = \frac{\sigma^{2}}{2k_0T}$$

(5)

and Δt is the timestep and $\theta_{ij}(t)$ is a symmetric random number. Note that w^D and w^R are weight functions that must relate by:

$$w^{*}(r_{ij}) = [w^{+}(r_{ij})]^{2} = \begin{cases} 1 - \frac{r_{ij}}{r_c}, & r_{ij} < r_c \\ 0, & r_{ij} > r_c \end{cases}$$

(6)

In addition to the three component non-bonded force, there is an additional force for the connected beads that form the polymer, F^{S}_{ij}. This is a harmonic spring type interaction that follows:

$$F_{ij}^{s} = Cr_{ij}$$

(7)

where C is the spring constant.

To use DPD for this specific material, a combination of two approaches was utilized to predict the morphology of the material assembly. Svaneborg demonstrated that dynamic bonding and DPD could be used to model DNA, while Li et al. established that electrostatics could be calculated implicitly using the novel Implicit Solvent Ionic Strength method (ISIS-

DPD).[65,66] The means of dynamic bonding used in this approach is based on a two-bead model resolution of DNA, where the phosphate and sugar ring is comprised of one bead and the other is the nucleobase. When two complimentary bases are within the cutoff distance of each other, they will form a bond as described in **Equation 7**, ultimately forming the assembled dsDNA. To compliment the dynamic bonding, using the ISIS-DPD approach the salt conditions of the solution can be scanned as a function of DNA length to predict the resulting morphology. This unique combination of two DPD centric methods allows for the assembly of these materials to be modeled and provide insight into the role of the solvent's impact on morphology.

The computational calculations of DPD were conducted using the molecular dynamics simulator, LAMMPS.[67] The initial system consists of 24 quantum dots distributed within a $40r$-x$40r$-x$40r$- periodic box. Each dot is decorated with 12 ssDNAs of varying length: 5, 10, 15, and 20 nucleobases. In other words, the system starts initially in a disassembled state and is iterated for 3 million timesteps resulting in the decorated quantum dots assembled via complimentary base pairing. Of the 24 quantum dots, 12 were decorated with base pair type A and 12 were decorated with complimentary base pair type B. An example of the initial system can be seen in **Figure 3A**. The interactions within the system are comprised of the non-bonded interactions described in **Equation 1**, the bonded interactions within the DNA and complimentary base pairs, and two angular harmonic potentials dictated by

$$E = K(\theta - \theta_1)^{\$} \tag{8}$$

where $K$is two times the harmonic prefactor, $\theta$is the angle at the time of calculation, and θ_0 is the equilibrium value of the angle. To reflect the physical orientation of DNA, the angles within the backbone beads comprised of the phosphate and sugar ring, K=20 and θ_0=150 degrees. The angle between the nucleobases and the backbone were, K=15 and θ_0=100 degrees. These angles were chosen based on mapping the center of masses of each resolved

bead on an atomic weight scale calculation. The bonded interactions established in **Equation 8** were harmonically set to C=200 with an equilibrium distance of 0. The a_{ij}interactions established in **Equation 2** are referenced in **Table 1**. The bead comprised of the phosphate and sugar ring is referred to as the backbone bead.

Table 1. Non-bonded interactions.

Interaction Description	a_{ij}
backbone to backbone	Varied from 25-90
backbone to nucleobases	40
backbone to QD	27
backbone to water	25
nucleobase type A to type A	22
nucleobase type A to type B	5
nucleobase to QD	27
nucleobase to water	27
water to water	25

Lastly, the QD core was comprised of 162 beads that were fix grouped, meaning that for each QD, the forces exerted on each individual bead were distributed throughout the entire core. This results in a fixed dot that consists of beads moving in concert with each other. Since computational modeling was conducted, calculations that quantify the morphological differences were conducted including the integration of the radial distribution functions (int-RDF). The int-RDF is a convenient method to describe the spatial relative positioning between the QDs.

Cell culture: Dr. Viard The human breast cancer cell line MDA-MB-231(with or without GFP) was maintained in DMEM, 10% heat-inactivated fetal bovine serum (FBS), and 1% PenStrep in incubators at 37 °C, 5% CO_2.

Uptake and co-localization: Dr. Viard Lipofectamine™ 2000 (L2K) was used for all experiments according to the manufacturer's guidelines.

Silencing assays: Dr. Viard For silencing experiments, cells were visualized using a UV 510 confocal microscope (Carl Zeiss, Oberkochen) and a Plan-Neofluar 40×/1.3 Oil lens. Flow cytometry was performed on a BD Accuri C6 flow cytometer; CellQuest or the CFlow Sampler software was used to retrieve the geometric mean fluorescence intensity (gMFI) and the standard error of the mean (SEM).

Immune stimulation by ELISA: Dr. Johnson hHμ and U87 cells were seeded at 1.5×10^5 cells/well in 12-well plates 24 hours prior to transfection. For final concentrations of 5, 10, 20, or 50 nM of each sample per well, 3 μL of L2K were used per treated well. OPTI-MEM was incubated separately with each sample and with total L2K for 5 minutes at room temperature. Afterwards, samples in OPTI-MEM were added to L2K in OPTI-MEM and incubated for 30 minutes at room temperature. Media was aspirated from the wells of each plate and replaced with 250 μL media + 250 μL of sample with L2K which was left to incubate at 37 °C, 5% CO_2 for 4 hours. Afterwards, media was aspirated and replaced with 1 mL of fresh media. Cells were incubated for an additional 20 hours before cell supernatants were collected and stored at -80 °C until analysis.

For each graph, the relative amount of cytokine production was normalized to the L2K-only treatment. To determine statistical significance, treatments were compared to L2K-only using a one-way ANOVA followed by Dunnett's multiple comparisons test performed in GraphPad Prism version 9.0.0 for Windows, GraphPad Software, San Diego, California USA, www.graphpad.com. All graphs show means of at least n=3 repeats ± SEM. A p-value of < 0.05 was considered statistically significant.

Supporting Information
Supporting Information is available from the Wiley Online Library or from the author.

Acknowledgements
Research reported in this publication was supported by the National Institute Of General Medical Sciences of the National Institutes of Health under Award Numbers R01GM120487 and R35GM139587 (to K.A.A). The content is solely the responsibility of the authors and does not necessarily represent the official views of the National Institutes of Health. The authors would like to thank Prof. Marcus Jones for helpful discussions at the early stages of this work. The authors would also like to thank Jose Castaneda (UNC Charlotte) and Brian Lynch (NCSU) for their contributions to the preliminary work on this project.

Received: ((will be filled in by the editorial staff))
Revised: ((will be filled in by the editorial staff))
Published online: ((will be filled in by the editorial staff))

References

1 Harold, F. M. Molecules into cells: specifying spatial architecture. *Microbiol. Mol. Biol. Rev.* **69**, 544-564, doi:10.1128/MMBR.69.4.544-564.2005 (2005).
2 Tamerler, C. & Sarikaya, M. Molecular biomimetics: nanotechnology and bionanotechnology using genetically engineered peptides. *Philos T R Soc A* **367**, 1705-1726, doi:10.1098/rsta.2009.0018 (2009).
3 Rosi, N. L., Thaxton, C. S. & Mirkin, C. A. Control of nanoparticle assembly by using DNA-modified diatom templates. *Angew Chem Int Edit* **43**, 5500-5503, doi:10.1002/anie.200460905 (2004).
4 Berry, V., Rangaswamy, S. & Saraf, R. F. Highly selective, electrically conductive monolayer of nanoparticles on live bacteria. *Nano Lett* **4**, 939-942, doi:10.1021/nl0495716 (2004).
5 Dujardin, E., Peet, C., Stubbs, G., Culver, J. N. & Mann, S. Organization of metallic nanoparticles using tobacco mosaic virus templates. *Nano Lett* **3**, 413-417, doi:10.1021/nl034004o (2003).
6 Kahn, J. S., Minevich, B. & Gang, O. Three-dimensional DNA-programmable nanoparticle superlattices. *Current Opinion in Biotechnology* **63**, 142-150, doi:https://doi.org/10.1016/j.copbio.2019.12.025 (2020).
7 Chen, D., Zhao, M. & Mundy, G. R. Bone morphogenetic proteins. *Growth Factors* **22**, 233-241, doi:10.1080/08977190412331279890 (2004).
8 Moradian-Oldak, J. Protein-mediated enamel mineralization. *Front Biosci (Landmark Ed)* **17**, 1996-2023 (2012).
9 Chen, C. L., Zhang, P. & Rosi, N. L. A new peptide-based method for the design and synthesis of nanoparticle superstructures: construction of highly ordered gold nanoparticle double helices. *J Am Chem Soc* **130**, 13555-13557, doi:10.1021/ja805683r (2008).
10 Stearns, L. A., Chhabra, R., Sharma, J., Liu, Y., Petuskey, W. T., Yan, H. & Chaput, J. C. Template-Directed Nucleation and Growth of Inorganic Nanoparticles on DNA Scaffolds. *Angew Chem Int Edit* **48**, 8494-8496, doi:10.1002/anie.200903319 (2009).

11 Carter, J. D. & LaBean, T. H. Organization of Inorganic Nanomaterials via Programmable DNA Self-Assembly and Peptide Molecular Recognition. *Acs Nano* **5**, 2200-2205, doi:10.1021/nn1033983 (2011).
12 Laramy, C. R., O'Brien, M. N. & Mirkin, C. A. Crystal engineering with DNA. *Nat Rev Mater* **4**, 201-224, doi:10.1038/s41578-019-0087-2 (2019).
13 Stewart, J. M., Viard, M., Subramanian, H. K., Roark, B. K., Afonin, K. A. &Franco, E. Programmable RNA microstructures for coordinated delivery of siRNAs. *Nanoscale* **8**, 17542-17550, doi:10.1039/c6nr05085a (2016).
14 Delebecque, C. J., Lindner, A. B., Silver, P. A. & Aldaye, F. A. Organization of intracellular reactions with rationally designed RNA assemblies. *Science* **333**, 470-474, doi:10.1126/science.1206938 (2011).
15 Sachdeva, G., Garg, A., Godding, D., Way, J. C. & Silver, P. A. In vivo co-localization of enzymes on RNA scaffolds increases metabolic production in a geometrically dependent manner. *Nucleic Acids Res* **42**, 9493-9503, doi:10.1093/nar/gku617 (2014).
16 Liu, X., Yan, H., Liu, Y. & Chang, Y. Targeted cell-cell interactions by DNA nanoscaffold-templated multivalent bispecific aptamers. *Small* **7**, 1673-1682, doi:10.1002/smll.201002292 (2011).
17 Panigaj, M., Johnson, M. B., Ke, W., McMillan, J., Goncharova, E. A., Chandler, M. & Afonin, K. A. J. A. n. Aptamers as modular components of therapeutic nucleic acid nanotechnology. **13**, 12301-12321 (2019).
18 Rackley, L., Stewart, J. M., Salotti, J., Krokhotin, A., Shah, A., Halman, J., Juneja, R., Smollett, J., Roark, B., Viard, M., Tarannum, M., Vivero-Escoto, J. L., Johnson, P., Dobrovolskaia, M. A., Dokholyan, N. V., Franco, E. & Afonin, K. A. RNA Fibers as Optimized Nanoscaffolds for siRNA Coordination and Reduced Immunological Recognition. *Adv Funct Mater*, doi:10.1002/adfm.201805959 (2018).
19 Achenbach, J. C., Nutiu, R. & Li, Y. Structure-switching allosteric deoxyribozymes. *Analytica Chimica Acta* **534**, 41-51, doi:10.1016/j.aca.2004.03.080 (2005).
20 Bath, J., Green, S. J. & Turberfield, A. J. A free-running DNA motor powered by a nicking enzyme. *Angew. Chem. Int. Ed. Engl.* **44**, 4358-4361, doi:10.1002/anie.200501262 (2005).
21 Liu, X., Lu, C.-H. & Willner, I. Switchable reconfiguration of nucleic acid nanostructures by stimuli-responsive DNA machines. *Acc. Chem. Res.* **47**, 1673-1680, doi:10.1021/ar400316h (2014).
22 Yurke, B., Turberfield, A. J., Mills, A. P., Simmel, F. C. & Neumann, J. L. A DNA-fuelled molecular machine made of DNA. *Nature* **406**, 605-608, doi:10.1038/35020524 (2000).
23 Modi, S., M G, S., Goswami, D., Gupta, G. D., Mayor, S. & Krishnan, Y. A DNA nanomachine that maps spatial and temporal pH changes inside living cells. *Nat Nanotechnol* **4**, 325-330, doi:10.1038/nnano.2009.83 (2009).
24 Zhou, M., Liang, X., Mochizuki, T. & Asanuma, H. A light-driven DNA nanomachine for the efficient photoswitching of RNA digestion. *Angew. Chem. Int. Ed. Engl.* **49**, 2167-2170, doi:10.1002/anie.200907082 (2010).
25 Halman, J. R., Satterwhite, E., Roark, B., Chandler, M., Viard, M., Ivanina, A., Bindewald, E., Kasprzak, W. K., Panigaj, M., Bui, M. N., Lu, J. S., Miller, J., Khisamutdinov, E. F., Shapiro, B. A., Dobrovolskaia, M. A. & Afonin, K. A. Functionally-interdependent shape-switching nanoparticles with controllable properties. *Nucleic Acids Res* **45**, 2210-2220, doi:10.1093/nar/gkx008 (2017).
26 Ke, W., Hong, E., Saito, R. F., Rangel, M. C., Wang, J., Viard, M., Richardson, M., Khisamutdinov, E. F., Panigaj, M., Dokholyan, N. V., Chammas, R., Dobrovolskaia, M. A. & Afonin, K. A. RNA-DNA fibers and polygons with controlled

immunorecognition activate RNAi, FRET and transcriptional regulation of NF-kappaB in human cells. *Nucleic Acids Res*, doi:10.1093/nar/gky1215 (2018).
27 Kahn, J. S., Hu, Y. & Willner, I. Stimuli-Responsive DNA-Based Hydrogels: From Basic Principles to Applications. *Acc. Chem. Res.* **50**, 680-690, doi:10.1021/acs.accounts.6b00542 (2017).
28 Mirkin, C. A., Letsinger, R. L., Mucic, R. C. & Storhoff, J. J. A DNA-based method for rationally assembling nanoparticles into macroscopic materials. *Nature* **382**, 607-609, doi:10.1038/382607a0 (1996).
29 Park, S. Y., Lytton-Jean, A. K. R., Lee, B., Weigand, S., Schatz, G. C. & Mirkin, C. A. DNA-programmable nanoparticle crystallization. *Nature* **451**, 553-556, doi:10.1038/nature06508 (2008).
30 Xu, X. Y., Rosi, N. L., Wang, Y. H., Huo, F. W. & Mirkin, C. A. Asymmetric functionalization of gold nanoparticles with oligonucleotides. *Journal of the American Chemical Society* **128**, 9286-9287, doi:10.1021/ja061980b (2006).
31 Cutler, J. I., Auyeung, E. & Mirkin, C. A. Spherical Nucleic Acids. *Journal of the American Chemical Society* **134**, 1376-1391, doi:10.1021/ja209351u (2012).
32 Matea, C. T., Mocan, T., Tabaran, F., Pop, T., Mosteanu, O., Puia, C., Iancu, C. & Mocan, L. Quantum dots in imaging, drug delivery and sensor applications. *Int J Nanomedicine* **12**, 5421-5431, doi:10.2147/IJN.S138624 (2017).
33 Tikhomirov, G., Hoogland, S., Lee, P. E., Fischer, A., Sargent, E. H. & Kelley, S. O. DNA-based programming of quantum dot valency, self-assembly and luminescence. *Nat Nanotechnol* **6**, 485-490, doi:10.1038/Nnano.2011.100 (2011).
34 Freeman, R., Girsh, J. & Willner, I. Nucleic acid/quantum dots (QDs) hybrid systems for optical and photoelectrochemical sensing. *ACS Appl Mater Interfaces* **5**, 2815-2834, doi:10.1021/am303189h (2013).
35 Martynenko, I. V., Litvin, A. P., Purcell-Milton, F., Baranov, A. V., Fedorov, A. V. & Gun'ko, Y. K. Application of semiconductor quantum dots in bioimaging and biosensing. *J Mater Chem B* **5**, 6701-6727, doi:10.1039/c7tb01425b (2017).
36 Gill, R., Zayats, M. & Willner, I. Semiconductor quantum dots for bioanalysis. *Angew Chem Int Ed Engl* **47**, 7602-7625, doi:10.1002/anie.200800169 (2008).
37 Michalet, X., Pinaud, F. F., Bentolila, L. A., Tsay, J. M., Doose, S., Li, J. J., Sundaresan, G., Wu, A. M., Gambhir, S. S. & Weiss, S. Quantum dots for live cells, in vivo imaging, and diagnostics. *Science* **307**, 538-544, doi:10.1126/science.1104274 (2005).
38 Opazo, F., Eiden, L., Hansen, L., Rohrbach, F., Wengel, J., Kjems, J. & Mayer, G. Modular Assembly of Cell-targeting Devices Based on an Uncommon G-quadruplex Aptamer. *Mol Ther Nucleic Acids* **4**, e251, doi:10.1038/mtna.2015.25 (2015).
39 Wen, L., Qiu, L., Wu, Y., Hu, X. & Zhang, X. Aptamer-Modified Semiconductor Quantum Dots for Biosensing Applications. *Sensors (Basel)* **17**, doi:10.3390/s17081736 (2017).
40 Shin, S., Kim, I. H., Kang, W., Yang, J. K. & Hah, S. S. An alternative to Western blot analysis using RNA aptamer-functionalized quantum dots. *Bioorg Med Chem Lett* **20**, 3322-3325, doi:10.1016/j.bmcl.2010.04.040 (2010).
41 Ma, Y., Wang, M., Li, W., Zhang, Z., Zhang, X., Tan, T., Zhang, X. E. & Cui, Z. Live cell imaging of single genomic loci with quantum dot-labeled TALEs. *Nat Commun* **8**, 15318, doi:10.1038/ncomms15318 (2017).
42 Ma, Y. X., Wang, M. X., Li, W., Zhang, Z. P., Zhang, X. W., Wu, G. Q., Tan, T. W., Cui, Z. Q. & Zhang, X. E. Live Visualization of HIV-1 Proviral DNA Using a Dual-Color-Labeled CRISPR System. *Anal Chem* **89**, 12896-12901, doi:10.1021/acs.analchem.7b03584 (2017).

43 Bentzen, E. L., House, F., Utley, T. J., Crowe, J. E., Jr. & Wright, D. W. Progression of respiratory syncytial virus infection monitored by fluorescent quantum dot probes. *Nano Lett* **5**, 591-595, doi:10.1021/nl048073u (2005).
44 Agrawal, A., Tripp, R. A., Anderson, L. J. & Nie, S. Real-time detection of virus particles and viral protein expression with two-color nanoparticle probes. *J Virol* **79**, 8625-8628, doi:10.1128/JVI.79.13.8625-8628.2005 (2005).
45 Joo, K. I., Lei, Y. N., Lee, C. L., Lo, J., Xie, J. S., Hamm-Alvarez, S. F. & Wang, P. Site-specific labeling of enveloped viruses with quantum dots for single virus tracking. *Acs Nano* **2**, 1553-1562, doi:10.1021/nn8002136 (2008).
46 Chen, Y. H., Wang, C. H., Chang, C. W. & Peng, C. A. In situ formation of viruses tagged with quantum dots. *Integr Biol (Camb)* **2**, 258-264, doi:10.1039/b926852a (2010).
47 Qin, C., Li, W., Li, Q., Yin, W., Zhang, X., Zhang, Z., Zhang, X. E. & Cui, Z. Real-time dissection of dynamic uncoating of individual influenza viruses. *Proc Natl Acad Sci U S A* **116**, 2577-2582, doi:10.1073/pnas.1812632116 (2019).
48 Srinivasan, C., Lee, J., Papadimitrakopoulos, F., Silbart, L. K., Zhao, M. & Burgess, D. J. Labeling and intracellular tracking of functionally active plasmid DNA with semiconductor quantum dots. *Mol Ther* **14**, 192-201, doi:10.1016/j.ymthe.2006.03.010 (2006).
49 Bhatia, D., Arumugam, S., Nasilowski, M., Joshi, H., Wunder, C., Chambon, V., Prakash, V., Grazon, C., Nadal, B., Maiti, P. K., Johannes, L., Dubertret, B. & Krishnan, Y. Quantum dot-loaded monofunctionalized DNA icosahedra for single-particle tracking of endocytic pathways. *Nat Nanotechnol*, doi:10.1038/nnano.2016.150 (2016).
50 Goryacheva, O. A., Mishra, P. K. & Goryacheva, I. Y. Luminescent quantum dots for miRNA detection. *Talanta* **179**, 456-465, doi:10.1016/j.talanta.2017.11.011 (2018).
51 Yuan, R., Yu, X. L., Zhang, Y. H., Xu, L. L., Cheng, W., Tu, Z. G. & Ding, S. J. Target-triggered DNA nanoassembly on quantum dots and DNAzyme-modulated double quenching for ultrasensitive microRNA biosensing. *Biosens Bioelectron* **92**, 342-348, doi:10.1016/j.bios.2016.11.002 (2017).
52 Jie, G. F., Zhao, Y., Wang, X. C. & Ding, C. F. Multiplexed fluorescence detection of microRNAs based on novel distinguishable quantum dot signal probes by cycle amplification strategy. *Sensor Actuat B-Chem* **252**, 1026-1034, doi:10.1016/j.snb.2017.06.107 (2017).
53 He, X., Zeng, T., Li, Z., Wang, G. & Ma, N. Catalytic Molecular Imaging of MicroRNA in Living Cells by DNA-Programmed Nanoparticle Disassembly. *Angew Chem Int Ed Engl* **55**, 3073-3076, doi:10.1002/anie.201509726 (2016).
54 He, X. W., Li, Z., Chen, M. Z. & Ma, N. DNA-Programmed Dynamic Assembly of Quantum Dots for Molecular Computation. *Angew Chem Int Edit* **53**, 14447-14450, doi:10.1002/anie.201408479 (2014).
55 Efros, A. L. & Nesbitt, D. J. Origin and control of blinking in quantum dots. *Nat Nanotechnol* **11**, 661-671, doi:10.1038/nnano.2016.140 (2016).
56 Roark, B. K., Tan, L. A., Ivanina, A., Chandler, M., Castaneda, J., Kim, H. S., Jawahar, S., Viard, M., Talic, S., Wustholz, K. L., Yingling, Y. G., Jones, M. & Afonin, K. A. Fluorescence blinking as an output signal for biosensing. *ACS sensors* **1**, 1295-1300 (2016).
57 Lim, E. K., Kim, T., Paik, S., Haam, S., Huh, Y. M. & Lee, K. Nanomaterials for Theranostics: Recent Advances and Future Challenges. *Chem Rev* **115**, 327-394, doi:DOI 10.1021/cr300213b (2015).
58 Bagalkot, V., Zhang, L., Levy-Nissenbaum, E., Jon, S., Kantoff, P. W., Langer, R. & Farokhzad, O. C. Quantum dot-aptamer conjugates for synchronous cancer imaging,

therapy, and sensing of drug delivery based on bi-fluorescence resonance energy transfer. *Nano Lett* **7**, 3065-3070, doi:10.1021/nl071546n (2007).
59 Chi, C. W., Lao, Y. H., Li, Y. S. & Chen, L. C. A quantum dot-aptamer beacon using a DNA intercalating dye as the FRET reporter: Application to label-free thrombin detection. *Biosens Bioelectron* **26**, 3346-3352, doi:10.1016/j.bios.2011.01.015 (2011).
60 Yang, L. T., Chueng, S. T. D., Li, Y., Patel, M., Rathnam, C., Dey, G., Wang, L., Cai, L. & Lee, K. B. A biodegradable hybrid inorganic nanoscaffold for advanced stem cell therapy. *Nature Communications* **9**, doi:ARTN 3147
10.1038/s41467-018-05599-2 (2018).
61 Espanol, P. & Warren, P. J. E. Statistical mechanics of dissipative particle dynamics. **30**, 191 (1995).
62 Warren, P. B. J. C. o. i. c. & science, i. Dissipative particle dynamics. **6**, 620-624 (1998).
63 Deaton, T. A., Aydin, F., Li, N. K., Chu, X., Dutt, M., Yingling, Y. G. J. F. o. M. M. & FOMMS, S. S. P. f. Dissipative Particle Dynamics Approaches to Modeling the Self-Assembly and Morphology of Neutral and Ionic Block Copolymers in Solution. 75.
64 Li, N. K., Fuss, W. H., Tang, L., Gu, R., Chilkoti, A., Zauscher, S. & Yingling, Y. G. J. S. M. Prediction of solvent-induced morphological changes of polyelectrolyte diblock copolymer micelles. **11**, 8236-8245 (2015).
65 Li, N. K., Fuss, W. H., Yingling, Y. G. J. M. T. & Simulations. An implicit solvent ionic strength (ISIS) method to model polyelectrolyte systems with dissipative particle dynamics. **24**, 7-12 (2015).
66 Svaneborg, C. J. C. P. C. LAMMPS framework for dynamic bonding and an application modeling DNA. **183**, 1793-1802 (2012).
67 Plimpton, S. J. J. o. c. p. Fast parallel algorithms for short-range molecular dynamics. **117**, 1-19 (1995).
68 Afonin, K. A., Viard, M., Martins, A. N., Lockett, S. J., Maciag, A. E., Freed, E. O., Heldman, E., Jaeger, L., Blumenthal, R. & Shapiro, B. A. Activation of different split functionalities upon re-association of RNA-DNA hybrids. *Nat Nanotechnol* **8**, 296-304, doi:10.1038/nnano.2013.44 (2013).
69 Schneider, C. A., Rasband, W. S. & Eliceiri, K. W. NIH Image to ImageJ: 25 years of image analysis. *Nature methods* **9**, 671-675, doi:10.1038/nmeth.2089 (2012).
70 Haeri, M. & Haeri, M. J. J. o. O. R. S. ImageJ plugin for analysis of porous scaffolds used in tissue engineering. **3** (2015).

*Morgan Chandler, Brandon Roark, Mathias Viard, Brian Minevich, M. Brittany Johnson, Mehedi Hasan Rizvi, Thomas A. Deaton, Seraphim Kozlov, Martin Panigaj, Joseph Tracy, Yaroslava G. Yingling, Oleg Gang, Kirill A. Afonin**

Controlled organization of inorganic materials using biological molecules for activating therapeutic functionalities

Supporting Information

Controlled organization of inorganic materials using biological molecules for activating therapeutic functionalities

*Morgan Chandler, Brandon Roark, Mathias Viard, Brian Minevich, M. Brittany Johnson, Mehedi Hasan Rizvi, Thomas A. Deaton, Seraphim Kozlov, Martin Panigaj, Joseph Tracy, Yaroslava G. Yingling, Oleg Gang, Kirill A. Afonin**

Sequences

DNA strands were designed to form RNA/DNA hybrids with sense and antisense strands of Dicer Substrate RNAs (DS RNAs) selected against Green Fluorescent Protein. Once formed, those hybrids have single-stranded DNA toeholds (underlined) which are designed to interact with each other to initiate branch migration.

DNA for Sense_12_Biotin
5'-/5Biosg/GGAGACCGTGACCGGTGGTGCAGATGAACTTCAGGGTCA

DNA for Antisense_12_Biotin
5'-/5Biosg/TGACCCTGAAGTTCATCTGCACCACCGGTCACGGTCTCC

RNA Sense
5'-/5Phos/ACCCUGAAGUUCAUCUGCACCACCG

RNA Antisense
5'-CGGUGGUGCAGAUGAACUUCAGGGUCA

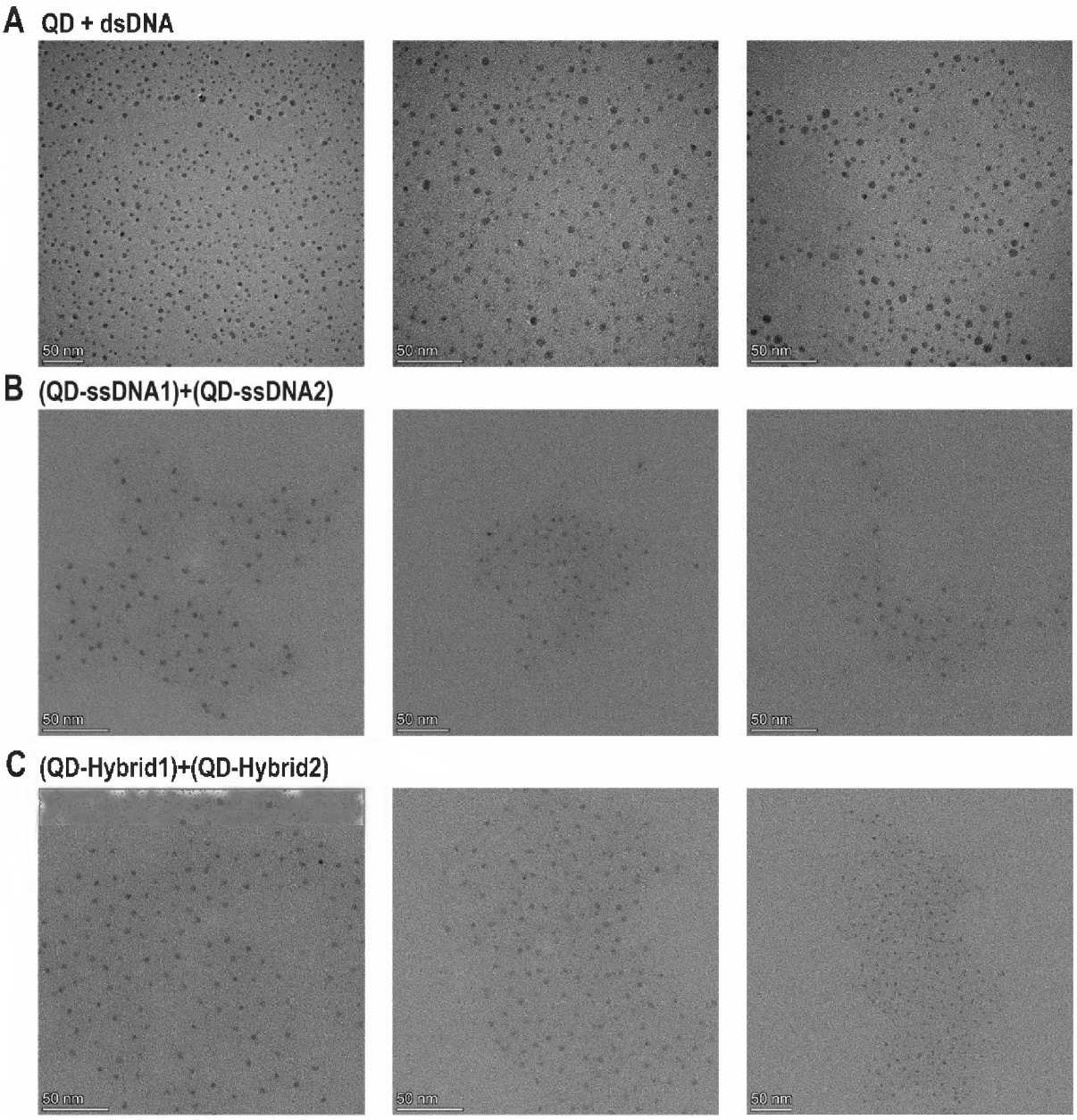

Figure S1. Three representative TEM images used for calculations of center-to-center distances in ImageJ. Lattices were formed via (**A**) QD+dsDNA, (**B**) (QD-ssDNA1)+(QD-ssDNA2), and (**C**) (QD-Hybrid1)+(QD-Hybrid2).

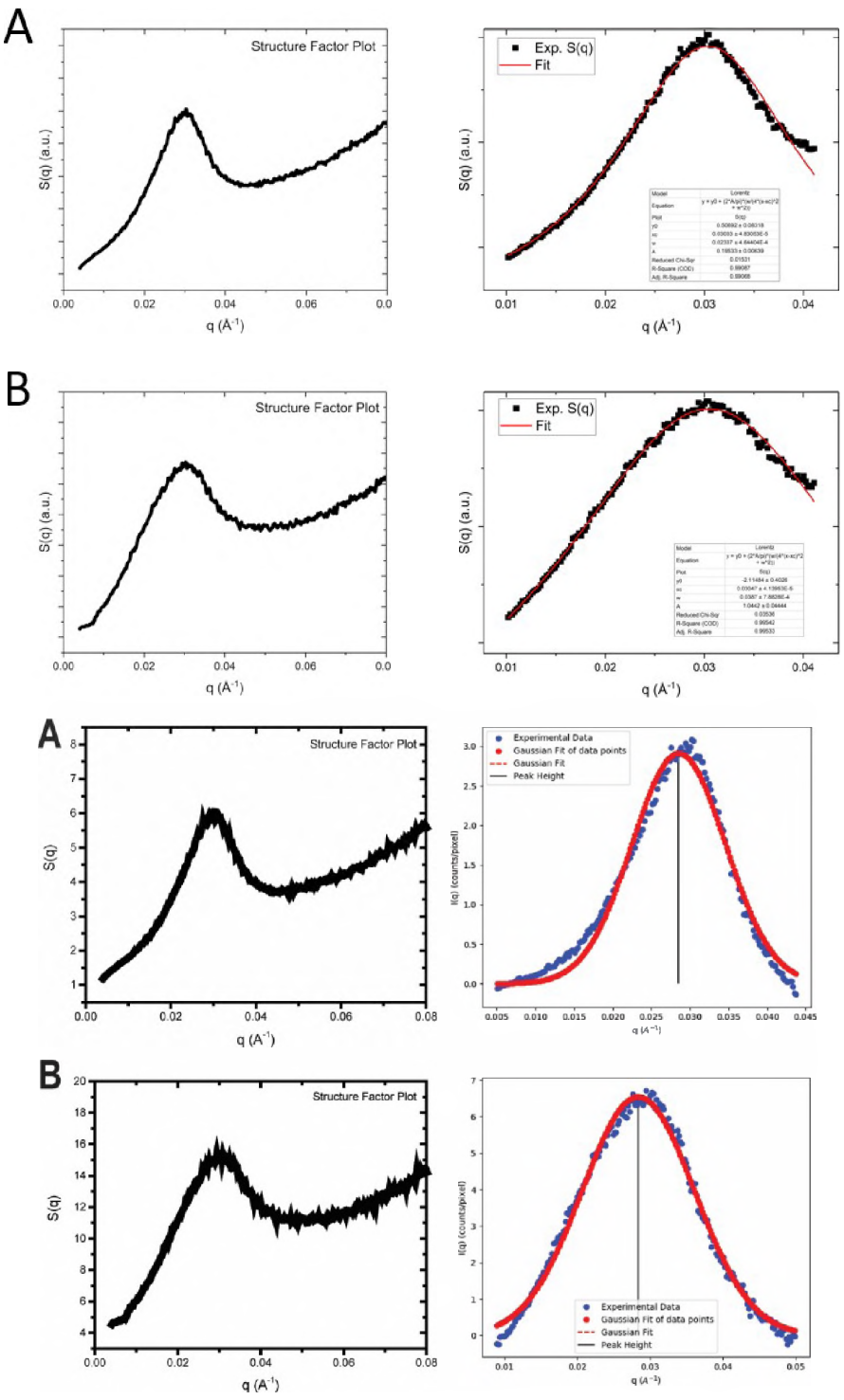

Figure S2. Additional SAXS analysis showing the Structure Factor Plot and Lorentzian Fit of two lattices: (**A**) QD+dsDNA and (**B**) (QD-Hybrid1)+(QD-Hybrid2).

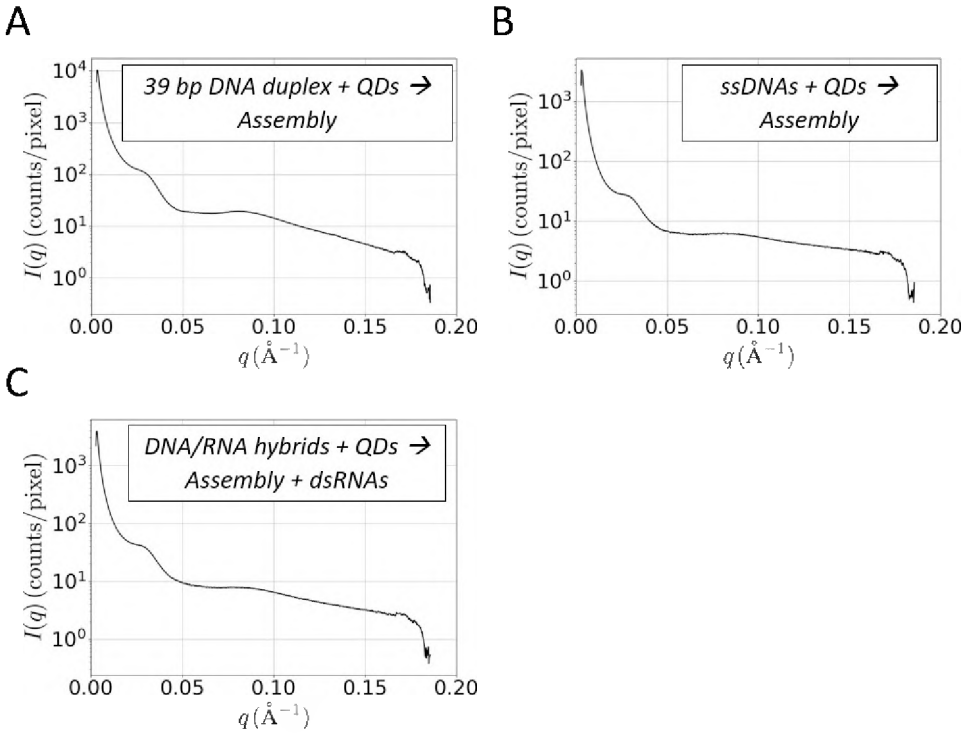

Figure S3. Intensity profiles, I(q), for each of the system designs described in Figures 1 and 2.

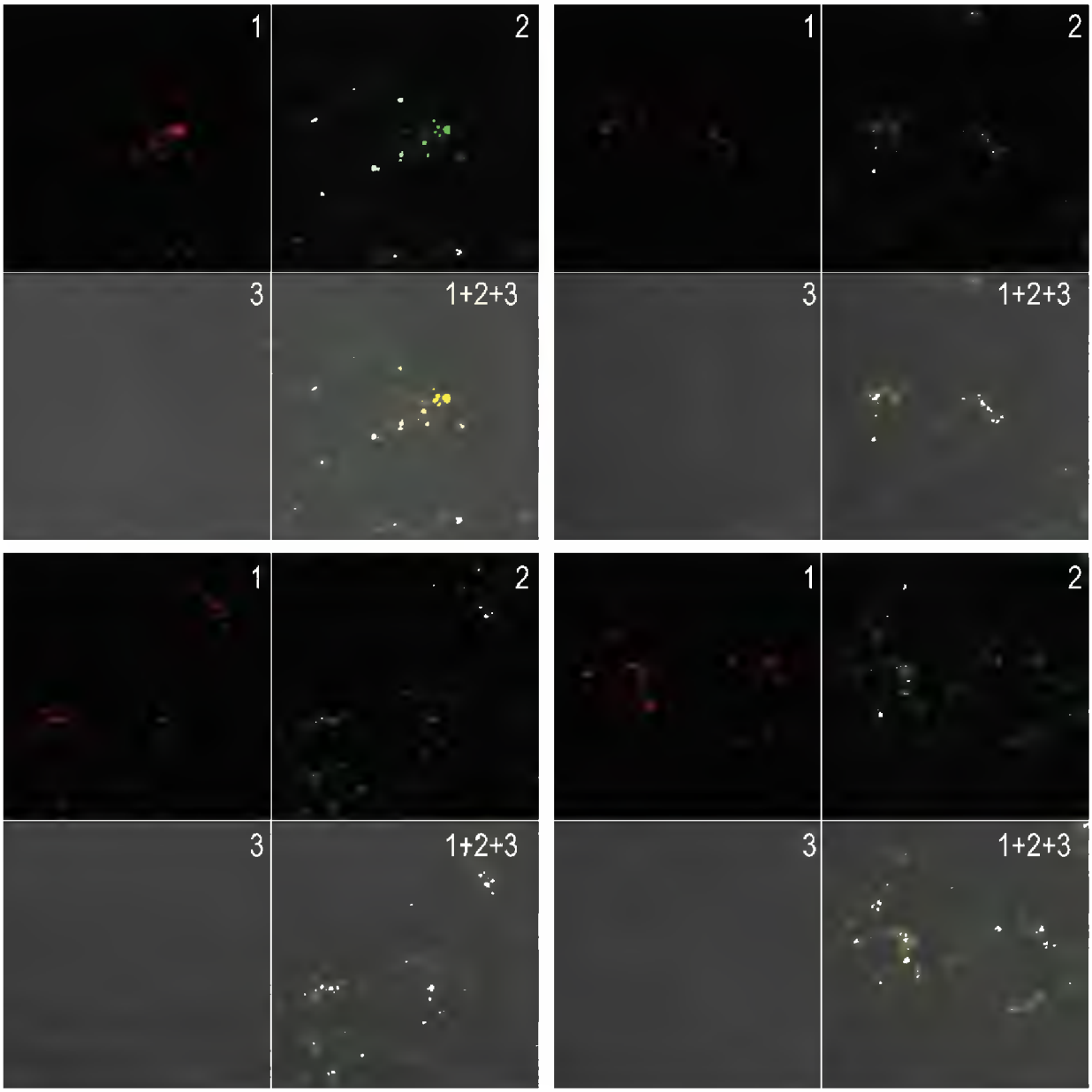

Figure S4. Co-localization of QD545 (green) and QD605 (red) entering the composition of formed intracellularly QD lattices analyzed by the confocal microscopy. Image numbers correspond to: QD605 emission (1), QD545 emission (2), and differential interference contrast (DIC) images (3). Images (1+2+3) are superposition of three different images.

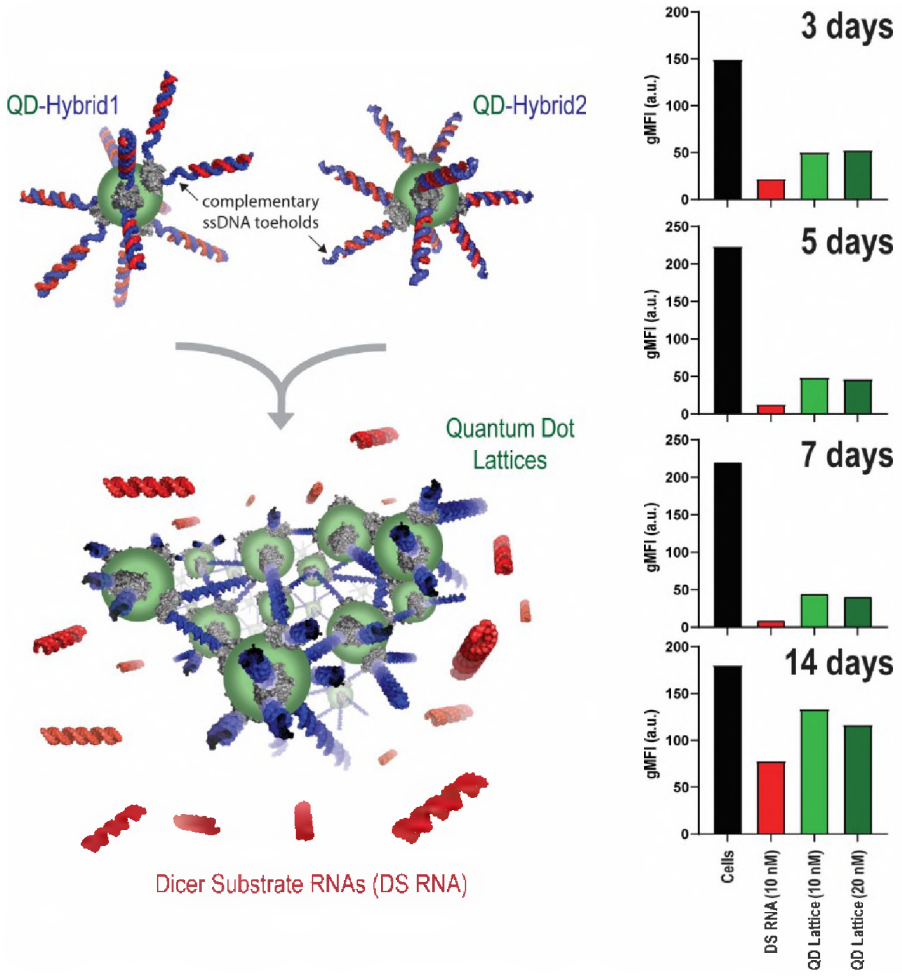

Figure S5. Activation of RNAi through QD lattice formation and release of DS RNAs using GFP knockdown assays for human breast cancer cells expressing GFP. Three, five, seven, and fourteen days after the co-transfection of cells with hybrid-functionalized QDs, GFP expression was analyzed with flow cytometry. As a control, transfections with the pre-formed DS RNA duplexes against GFP were used. gMFI corresponds to the geometric mean fluorescence intensity.

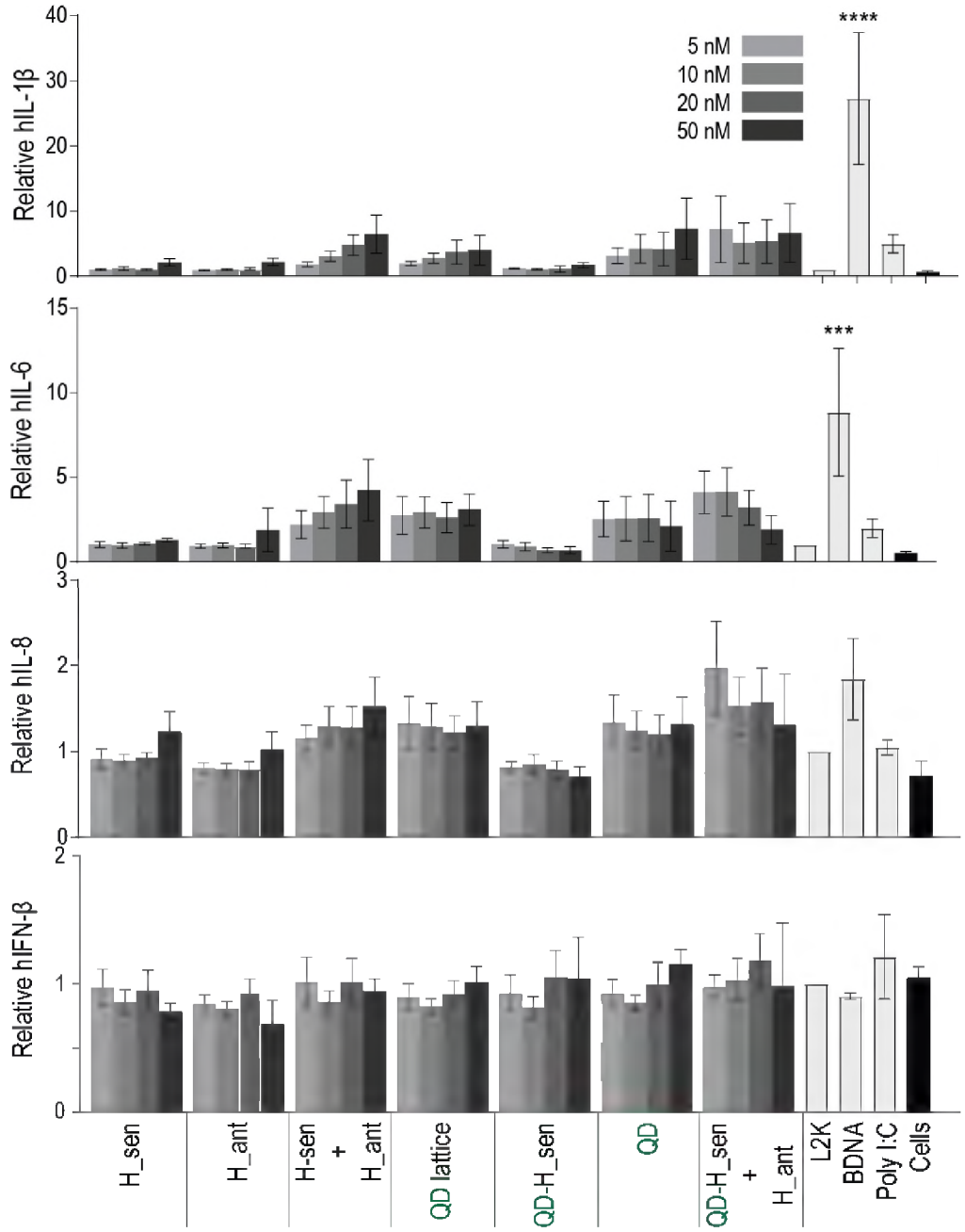

Figure S6. Immunostimulatory activity of QD lattices in the human astrocyte-like cell line U87. Cells were transfected and cell supernatants were collected 24 hours later. Levels of hIL-1β, hIL-6, hIL-8, and hIFN-β were assessed by specific-capture ELISA. Error bars denote ± SEM. Statistically significant results are indicated with asterisks (**** = p-value < 0.0001, *** = p-value <0.001).

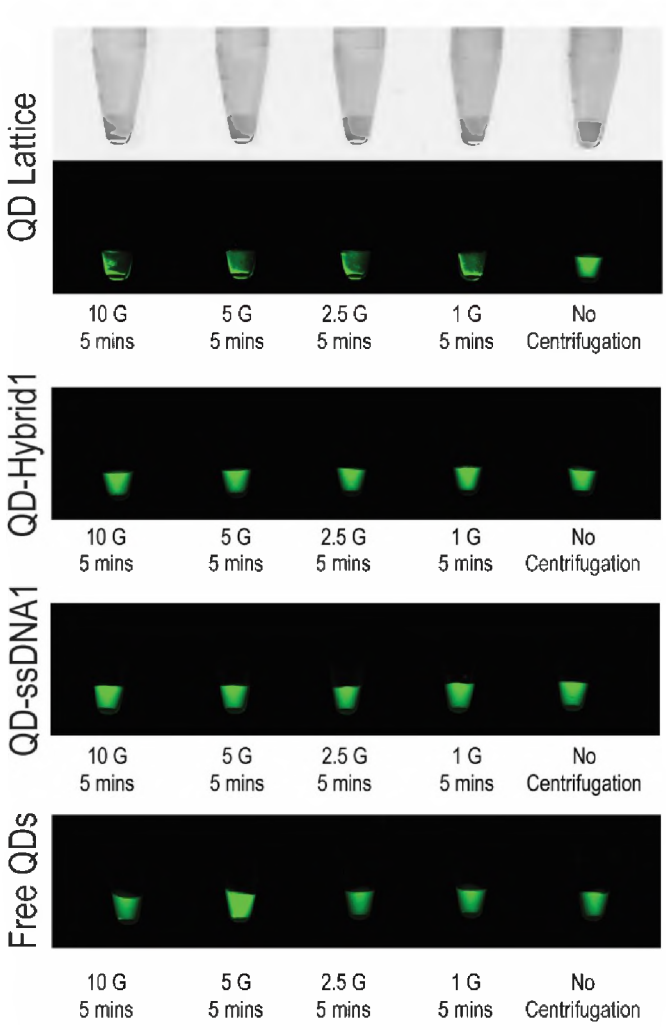

Figure S7. Precipitation of QD lattices. Assembled lattices were centrifuged for 5 minutes at various speeds and show the formation of a solid pellet in the bottom of the tube. For all other QD samples which are not assembled, no precipitation is observed.

Beamline	11-BM CMS
Photon Energy (keV)	13.5
Horizontal × Vertical Beam size (μm × μm)	200 x 200
Approximate Flux (photons/sec)	10^{11}
Sample-to-Detector Distance (m)	5.05
Detector Manufacturer	Dectris
Detector Model	Pilatus 1M
Detector Pixel Size (μm x μm)	172 x 172

Table S1. CMS Beamline Experimental Setup